



Nanorod β -Ga₂O₃ semiconductor modified activated carbon as catalyst for improving power generation of microbial fuel cell

Xiujuan Li^{1,2,3} · Di Liu^{1,2,3} · Xiaoping Mo^{1,2,3} · Kexun Li^{1,2,3}

Received: 10 March 2019 / Revised: 23 August 2019 / Accepted: 24 August 2019 / Published online: 7 September 2019
© Springer-Verlag GmbH Germany, part of Springer Nature 2019

Abstract

Nanorod monoclinic β -Ga₂O₃ semiconductor, synthesized by a facile hydrothermal method, was firstly researched as a catalyst to modify activated carbon air cathode in microbial fuel cells (MFCs). The maximum power density of modified MFC reaching $1843 \pm 40 \text{ mW m}^{-2}$ was 3 times higher than the control. The Brunauer-Emmett-Teller (BET), transmission electron microscope (TEM), and X-ray diffraction (XRD) results revealed the larger surface area and porous structure could provide more active sites to improve the performance of MFCs. The result of X-ray photoelectron spectroscopy (XPS) confirmed that plenty of oxygen vacancy existed in the synthesized β -Ga₂O₃. Tafel curve and rotating disk electrode (RDE) results illustrated the high exchange current density of β -Ga₂O₃ and the four-electron pathway at the cathode during the oxygen reduction reaction (ORR), respectively. The cathode modified with β -Ga₂O₃ displayed excellent improvement towards ORR and therefore improved the performance of MFCs.

Keywords β -Ga₂O₃ · Semiconductor · Oxygen vacancy · Oxygen reduction reaction · Microbial fuel cells

Introduction

MFCs are capable of converting inorganic and organic pollutions in wastewater into electrical energy, which could be a promising approach to obtaining a sustainable energy in the future [1, 2]. However, the oxygen reduction kinetics of cathode is a critical limiting factor influencing the performance of MFCs. Thus finding a highly active catalyst is of great necessity to promote the cathode reaction [3–5].

For a long time, platinum (Pt) has attracted much attention from scientists due to its excellent catalytic properties. However, its high cost holds back the practical application of Pt in MFCs. So it is imperative to find some alternatives to replace the platinum catalyst, and semiconductor nanomaterials are considered as great candidates because of large surface area, low electrical resistivity, outstanding electron transport properties, and good electrochemical properties [6, 7]. In recent years, some semiconductors have already been applied in MFCs, such as nano Fe₃O₄, N-type Cu₂O and carnation-like MnO₂, all of which showed excellent catalytic property [8–10].

Gallium oxide (Ga₂O₃) is a III-VI semiconductor which has been proven to be a promising efficient photocatalyst for application in high-power electronic devices [11]. The price of Ga₂O₃ is about 2.3 \$/g, much cheaper than Pt (66 \$/g). As a binary metal oxide, Ga₂O₃ is extraordinarily sensitive to oxygen [12]. Previous study demonstrated that adding Ga₂O₃ into electrochemical activated carbon could effectively prolong the cycle life of batteries [13]. Li et al. found that Ga₂O₃ displayed great catalytic activity in terms of the photocatalysis [14]. Wang et al. proved that the application of Ga₂O₃ in metal oxide semiconductor capacitor could improve its performance [15]. Even more, the Ga₂O₃ nanorods prepared via a facile hydrothermal followed by proper calcination exhibited a relatively high photocatalytic efficiency [16].

Xiujuan Li and Di Liu contributed equally to this work.

Electronic supplementary material The online version of this article (<https://doi.org/10.1007/s10008-019-04377-4>) contains supplementary material, which is available to authorized users.

✉ Xiaoping Mo
moxp@nankai.edu.cn

✉ Kexun Li
likx@nankai.edu.cn

¹ College of Environmental Science and Engineering, Nankai University, Tianjin 300071, China

² MOE Key Laboratory of Pollution Processes and Environmental Criteria, Nankai University, Tianjin 300071, China

³ Tianjin Key Laboratory of Environmental Remediation and Pollution Control, Tianjin 300071, China

Up to now, there are very few researches about the performance and mechanism of Ga_2O_3 as a highly active catalyst modified AC in air cathode MFCs. The nanorod monoclinic $\beta\text{-Ga}_2\text{O}_3$ was synthesized by a hydrothermal method in this study. The performance of $\beta\text{-Ga}_2\text{O}_3$ modified cathode is characterized by several electrochemical tests. According to Linear sweep voltammetry (LSV), open circuit potential was obtained. Electrochemical impedance spectroscopy (EIS) was used to analyze resistance of the cathode. Meanwhile, the electron transfer of the catalyst can be tested by RDE and Tafel plot. In order to explore the morphology and crystal structure of $\beta\text{-Ga}_2\text{O}_3$, some characterizations such as XRD, scanning electron microscopy (SEM), and TEM were performed. XPS was conducted to analyze chemical composition. Besides, surface area was demonstrated via BET.

Materials and methods

Synthesis of $\beta\text{-Ga}_2\text{O}_3$

The synthesis method of $\beta\text{-Ga}_2\text{O}_3$ referred to previous study [17]. Typically, adequate sodium dodecyl benzene sulfonate (SDBS) was added into the solution with $0.01 \text{ mol L}^{-1} \text{ Ga}^{3+}$, which formed by dissolving $\text{Ga}(\text{NO}_3)_3 \cdot n\text{H}_2\text{O}$ into deionized water. After that, the mixed liquor was treated by hydrothermal method in Teflon-lined stainless steel autoclaves at $140 \text{ }^\circ\text{C}$ for 12 h. Then, the product was washed with deionized water for several times after solid-liquid separation. The obtained solid product was heated at $900 \text{ }^\circ\text{C}$ in the muffle furnace for 5 h and then cooled down to $20 \text{ }^\circ\text{C}$.

Air cathode fabrication

Rolling method was used to construct air cathode as described previously [18]. There were three-phase interface in the air cathode, a stainless steel mesh, a gas diffusion layer (GDL) and a catalyst layer (CL). The GDL was made of carbon black (Jin Qiu Shi Chemistry Co. Ltd., Tianjin, China) and PTFE (60% wt%, Hesen, Shanghai, China) with a mass ratio of 3:7. Firstly, the carbon black and proper ethanol were put into a 100-mL beaker, and the mixture was shocked ultrasonically until that the ethanol was almost dried. Then the PTFE was added. When the mixture was like a past, it was rolled on one side of a stainless steel mesh. Then, it was heated at $340 \text{ }^\circ\text{C}$ for about 20 min to sinter and harden [19]. The CL was established by composites and PTFE with a mass ration of 6:1. The composites were made by adding different percentage (0 wt%, 3 wt%, 5 wt%, and 8 wt%) of the prepared $\beta\text{-Ga}_2\text{O}_3$ into the AC ($2100 \text{ m}^2 \text{ g}^{-1}$, Yihuan Carbon Co. Ltd., Fujian, China), namely RAW-AC, AC-G1, AC-G2, and AC-G3, respectively. The method of making a past for CL was the

same with the GDL, but it was rolled on the other side of the stainless steel mesh. Each cathode was prepared with three parallel samples. Finally, the cathode was put into biochemical incubator for 6 h.

MFC setup and operation

The single chamber MFC was composed of a cylindrical plexiglas chamber whose diameter and inner volume were 3 cm and 28 mL respectively [20]. The distance of both electrodes with effective area of 7 cm^2 was 4 cm. The embedded titanium wire was used to connect the anode and cathode. Anodes were made of carbon felt as previous studies [21, 22]. Herein, the organic matter and impurities of carbon felt were removed by means of immersing in acetone for 12 h. Meanwhile, lay-up overnight was beneficial for the hybrid biofilm to firmly adhere to the surface of carbon felt. Then the carbon felt was washed with deionized water before it was installed in the MFC [23]. The external resistance was $1000 \text{ } \Omega$. The nutrient solution included phosphate buffered saline (PBS 50 mM), trace minerals (12.5 mL L^{-1}), vitamins (5 mL L^{-1}), acetate solution (2 g L^{-1}), and waste water (Ji Zhuangzi sewage treatment plant, Tianjin China) in the first 3–4 cycles (1 cycle 1–2 days) of cell culture. The operation temperature of MFC was controlled at $30 \text{ }^\circ\text{C}$.

Electrochemical characterization

The external resistance was changed from 9000 to $50 \text{ } \Omega$ when measuring polarization and power density curves. It was necessary to test each resistor every 30 min, contributing to obtain a stable voltage. Ag/AgCl was used as reference electrode during the cathode and anode potentials polarization measurement. MFC must remain at open circuit potential (OCP) for 6 h to ensure the stability before testing. All the LSV, EIS and Tafel plot were tested in three electrode system, which included a reference electrode (Ag/AgCl), an auxiliary electrode (platinum sheet of 1 cm^2) and a working electrode (as-prepared cathode). The data were calibrated to RHE scale. Concretely, LSV was tested with scanning voltage from OCP to -0.1 V at a scan rate of 0.1 mV s^{-1} in 50 mM PBS. EIS was conducted over the frequency range from 10 kHz to 0.1 Hz at OCP [24]. Tafel plot was measured over potential from 200 to 300 mV, which could calculate the exchange current density (i_0) by the experience Tafel equation $\log i = \log i_0 - \beta n F \eta / 2.303 RT$ [25]. Rotating disk electrode (RRDE-3A, ALS, Japan) was used to assess the catalytic activity of the materials toward the ORR. The specific operation was the same as previous mentioned [26]. During the measurement, ultra-high pure O_2 was used as the decontaminant for the electrolyte, and the linear scanning voltage was changed from 0.5 to -0.8 V at a scan rate of 5 mV s^{-1} with the rotating speed from 625 to 2500 rpm.

XPS was conducted with an XPS spectrometer (K-Aepna, Thermo Fisher Scientific Inc., USA) to analyze elemental content and state. XRD was carried out on a D/max-2500 X-ray generator to explore the crystal structure of the β -Ga₂O₃. The 2-theta diffraction angle varied from 10 to 80° while the velocity was 0.02 min⁻¹. BET was performed with an adsorption meter (ASAP2020/Tristar 3000, MICROMERITICS) to measure the pore size distribution and specific surface. SEM equipped with an energy-dispersive X-ray spectrometer (S-3500N, Hitachi) and a JSM-7500F field emission transmission electron microscope (FE-TEM) were used for analyzing morphology and microstructure of the prepared β -Ga₂O₃. In TEM test, the point and linear resolution were 0.24 nm and 0.14 nm, respectively.

Results and discussion

Structural characterization

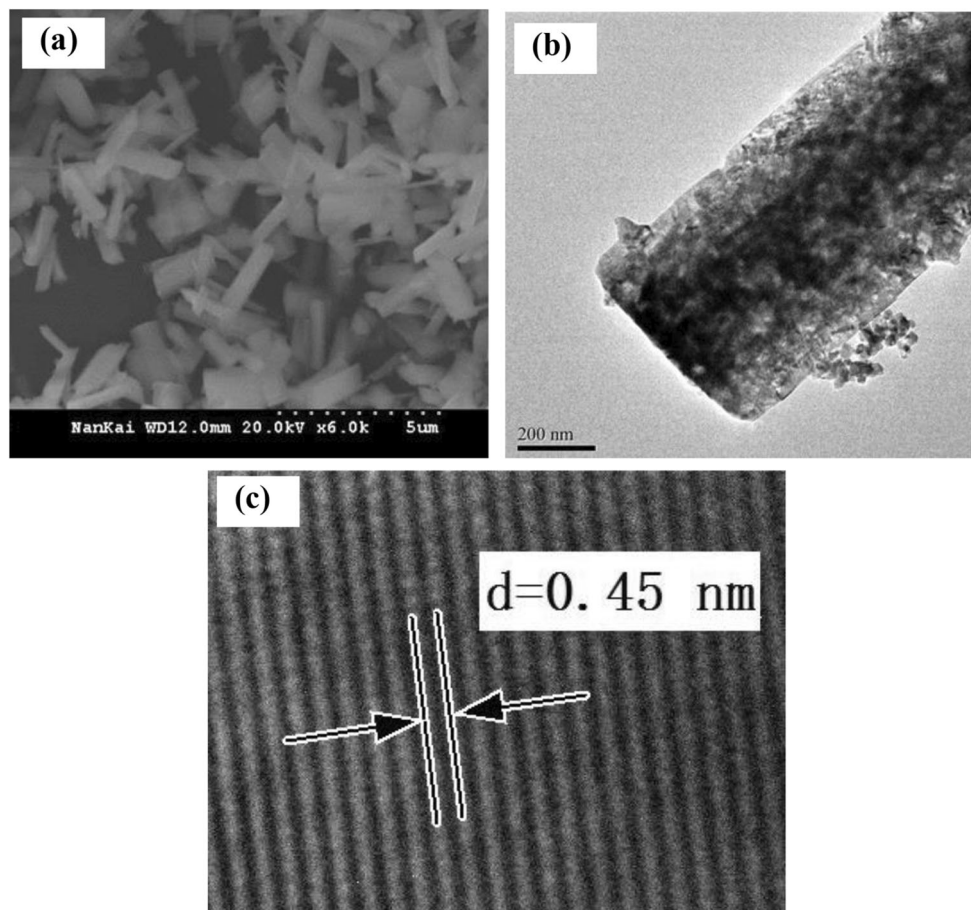
Figure S1 illustrated the typical XRD patterns of the sample. The lattice constants of the sample were $a = 12.23 \text{ \AA}$, $b = 3.04 \text{ \AA}$, $c = 5.80 \text{ \AA}$, and $\beta = 103.7^\circ$, in excellent agreement with the values of β -Ga₂O₃ in previous reports [27]. The result was in

accordance with the monoclinic β -Ga₂O₃ phase with space group C2/m. The diffraction peaks corresponded to the (-201), (400), (002), (111), (-311), (600), (313), and (221) planes, respectively. The sharp diffraction peaks exposed that the prepared β -Ga₂O₃ had a high crystalline quality. The diffraction peak (111) showed high intensity for both the rods and nanostructures [28]. Moreover, no diffraction peaks from other impurities were found within the detection limit, illustrating the prepared material was the predominantly single β -Ga₂O₃ phase with high purity.

Figure 1a, b, and c showed the typical SEM and TEM images of β -Ga₂O₃. From Fig. 1a, numerous nanorods could be clearly observed. These nanorods exhibited different length and uneven thickness, and staggered with each other. The variations of the crystal shape and the size of β -Ga₂O₃ nano-composites were obtained through the present SEM data.

TEM images (Fig. 1b, c) revealed the surface morphology and microstructure of β -Ga₂O₃. The single β -Ga₂O₃ nanorod that exhibited a diameter of 500 nm with many nanoholes was obtained through the TEM images (Fig. 1b). The holes regarded as the channels for gaseous transport were formed along with the elimination of the water molecules, thus resulting in the creation of many vacancies (gallium vacancy (VGa) or gallium-oxygen vacancy pair (VGa-VO)) [29],

Fig. 1 The morphology of the catalyst. **a**, **b** SEM and TEM image of β -Ga₂O₃; **c** HRTEM image of the selected area



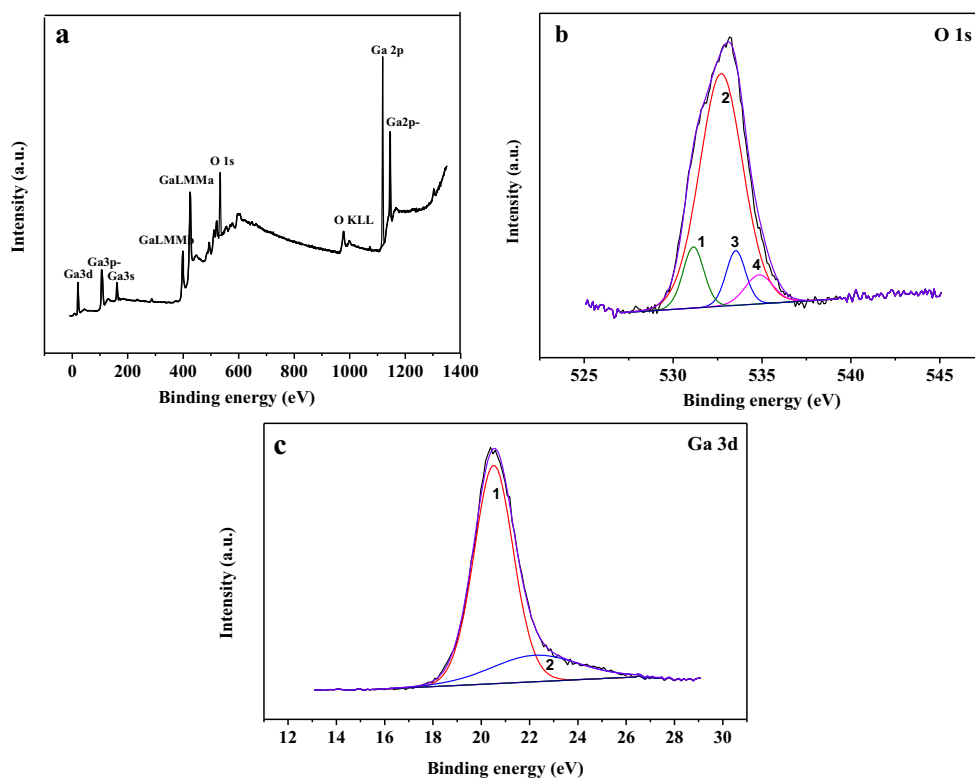
which could promote the catalytic activity [15, 30]. Besides, the rough surface of the nanorods (Fig. 1b) indicated a large specific surface area, which was beneficial to promote the electrocatalytic performance. And some nanoparticles could be observed at the bottom of the nanorod, which may be the particles that papered to form the nanorods but have not yet formed. According to the high-resolution TEM (HRTEM) images in Fig. 1c, the line array of lattice fringes measuring with a spacing of $d \approx 0.45$ nm was reasonable compared with the measured crystal plane of the corresponding XRD peak of (-201). The disordered nanorods were deemed to form more active heterogeneous catalysts, due to the easy accessibility of the guest molecules to active sites in multidimensional framework [31].

The specific surface areas and pore structure of the sample were characterized by BET, and the results were presented in Fig. S2. The isothermal profile was categorized as a typical Langmuir type III. The apparent hysteresis loop indicated the existence of mesoporous structure. From the insert image in Fig. S2, the average mesopore size was about 45 nm, similar to CoGa_2O_4 [32]. The mesopore enhanced diffusion of the reactants to the catalytic functional sites on the $\beta\text{-Ga}_2\text{O}_3$ doped AC. Meanwhile, the mesoporous structure also accelerated ORR by virtue of effective oxygen transportation [33]. Besides, the macroporous structure occupied a relatively large proportion with the pore size of 143 nm, which could guarantee efficient substrates transport, thus enhanced the electrochemical reaction. The hierarchical structure could make the

mass transport resistance lower and expose more ORR active sites, thus benefit ORR performance [34, 35]. The BET specific surface area of the prepared $\beta\text{-Ga}_2\text{O}_3$ was $117.2 \text{ m}^2 \text{ g}^{-1}$, larger than reported $\alpha\text{-Ga}_2\text{O}_3$ ($56 \text{ m}^2 \text{ g}^{-1}$), Ga_2O_3 synthesized by microwave refluxing ($66.5 \text{ m}^2 \text{ g}^{-1}$), and the nanocrystalline $\beta\text{-Ga}_2\text{O}_3$ ($84 \text{ m}^2 \text{ g}^{-1}$) [36–38]. The carbonaceous material cathode displayed excellent performance due to the high surface area. Similarly, the prepared $\beta\text{-Ga}_2\text{O}_3$ with high surface area could enhance the electrocatalytic performance of the cathodes [39].

The results of the chemical bonding state analysis of the prepared nanomaterials measured by XPS. The typical XPS survey spectrum (Fig. 2a) with energy ranging from 0 to 1400 eV revealed the peaks of the core level from Ga3d, Ga2p, and O1s states, respectively. In Fig. 2b, the O1s spectra showed the binding energy of four kinds of oxygen signals (O1, O2, O3, O4): 531.1 eV, 532.8 eV, 533.5 eV, and 534.8 eV, respectively. Figure 2c revealed the Ga-3d spectra was decomposed into two individual component peaks (Ga1, Ga2): located at 20.5 eV and 22.2 eV, respectively. Figure 2a showed the stem from Ga2p representing the Ga–O bonding with the oxygen vacancy site [40, 41]. Furthermore, the component 1 of O1s peak located at around 531.1 eV was corresponding to the lattice oxygen which was combined with an activation energy barrier (E_a) of 1.05 eV to release O_2 and leave oxygen vacancy, while the component 2 and component 3 of O1s peak at 532.8 eV and 533.5 eV were ascribed to H_2O accompanied by the presence of oxygen vacancies [41–43].

Fig. 2 XPS spectra of $\beta\text{-Ga}_2\text{O}_3$ material **a** Full spectrum diagram; **b** O1s core level and **c** Ga3d core level



The component 4 of O1s peak at 534.8 eV corresponded to the characteristic peaks of Ga–O. The position of the Ga3d binding energy peaks presented in Fig. 2c confirmed the presence of Ga₂O₃ [44]. The peak at around 20.5 eV was the characteristics of Ga³⁺ [32]. The energy peak of Ga3d was centered at around 22 eV which could be ascribed to the presence of gallium in β -Ga₂O₃ [28]. The slight right shift in the Ga3d binding energy peak suggested a slight oxygen deficiency [44].

The atomic ratio of Ga to O in β -Ga₂O₃ (0.91) that obtained from the XPS result was higher compared with the theoretical ratio (0.67), which could adequately prove the existence of oxygen vacancy. Moreover, β -Ga₂O₃ has the same atomic ratio of Ga to O as CoGa₂O₄ [32]. In generally, a number of previous studies have confirmed that moderate oxygen vacancies in oxides can improve electrocatalytic activity toward the ORR at room temperature [43]. The dissimilarity between the atomic ratio and theoretical ratio of Ga and O in β -Ga₂O₃ was 0.240, which was higher than that of non-stoichiometric nano Fe₃O₄ (0.189) [8]. The result revealed that more oxygen vacancies in the β -Ga₂O₃ could promote the performance toward the ORR. Oxygen vacancy could serve as electron acceptor and oxygen adsorbent, which could greatly enhance the catalytic properties [45]. As in previous report, oxygen vacancy density promoted activation of oxygen molecules into active oxygen adspecies, leading to better catalytic performance [46]. Also, the increased concentration of oxygen vacancies could lead to enhanced oxide-ionic conductivity [47]. Zheng et al. pointed out that the surface oxygen vacancy could serve as an efficient reductant [48]. Meanwhile, β -Ga₂O₃ existed amount of gallium vacancies which could provide more active sites [49]. In semiconducting oxides, adsorbed oxygen behaved as a surface acceptors state, further accepted electrons from the valence band and hence increased the electron concentration. Therefore, the much greater number of vacancies could contribute significantly to the excellent catalytic of β -Ga₂O₃.

Electrochemical analysis

LSV curve initially evaluated the effect of β -Ga₂O₃ on ORR and the result was shown in Fig. 3a. The most pivotal performance of these cathodes was dropped within the potential range of 0.1 to 0.3 V. Obviously, the current densities of the treated AC were remarkably increased compared with the control.

At the potential of 0.1 V, the highest current density received by AC-G2 was 7.016 mA cm⁻², 64.31% higher than that of RAW-AC electrode (4.270 mA cm⁻²). The current density at the potential of 0.1 V exhibited a positive trend: RAW-AC (4.270 mA cm⁻²) < AC-G3 (5.114 mA cm⁻²) < AC-G1 (6.350 mA cm⁻²) < AC-G2 (7.016 mA cm⁻²). The current densities of all the β -Ga₂O₃/AC air cathodes were

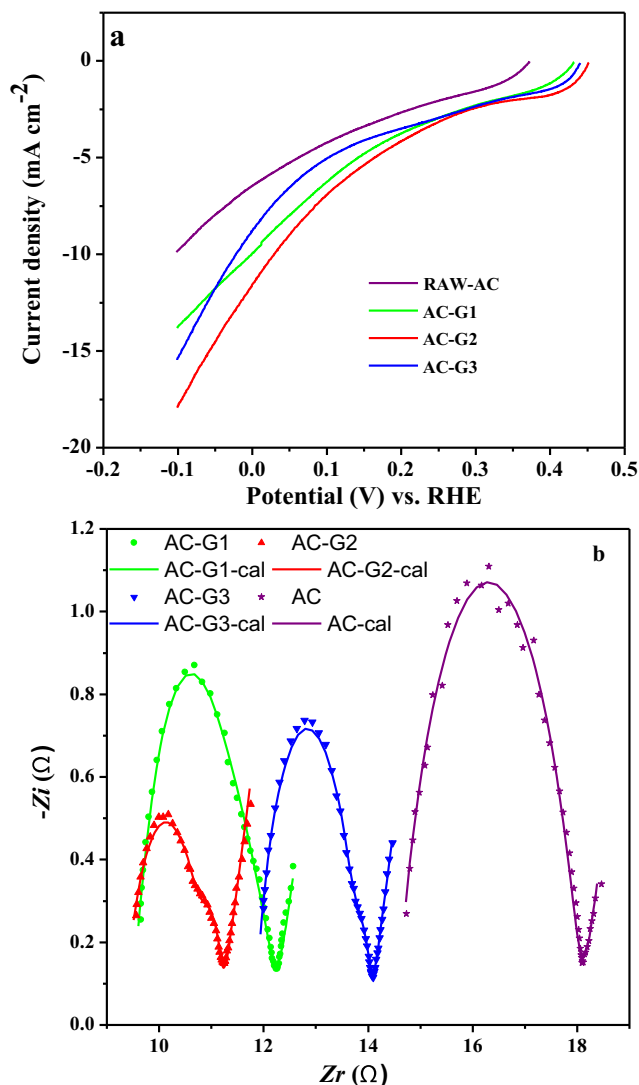


Fig. 3 a LSVs of different cathodes. b Nyquist plots of EIS of different cathodes. Lines marked as ‘Cal’ were fitting data from the equivalent circuit

distinctly higher than that of the RAW-AC. In addition, the current densities of nano Fe₃O₄ and Co/N-C air cathodes at the potential of 0.1 V were 6.87 mA cm⁻² and 6.17 mA cm⁻², respectively [8, 50], indicating that β -Ga₂O₃ was of benefit to the electrochemical activity.

To our knowledge, β -Ga₂O₃ behaves as an *n*-type semiconductor due to the presence of a donor band related to intrinsic oxygen deficiency [51]. In *n*-type semiconductor electrodes, the electron holes accumulate on the surface of the semiconductor and are consumed in oxidation reactions, while electrons are transferred to the electrode via the back contact and an external circuit, and used in reduction reactions [52]. The electron-hole pairs could enhance the catalytic efficiency [53]. Because of these characteristics, the β -Ga₂O₃ modified AC air cathode had high current density. The larger current density revealed that the β -Ga₂O₃ was an alternative to traditional Pt catalyst.

To further confirm the improved ORR performance and interpret the experimental results, EIS measurement data was shown in Fig. 3b. The equivalent circuit method was provided, which was shown in Fig. S3. The values of R_0 , R_d , R_{ct} , Q , C , and W represented ohmic resistance, diffusion resistance, charge transfer resistance, pore adsorption capacitance, double layer capacitance and War-burg impedance, and R_0 , R_d and R_{ct} were the focus of our work.

The results of the EIS of all the cathodes were shown in Fig. 3b and Table 1, from which we can see the total resistances (R_T) of all the modified cathodes displayed a significant decrease, which exerted positive effect on the increase of the power density. The R_T of AC-G2 was 11.157 Ω , lower than other cathodes and the traditional Pt/C electrode (16.4 Ω) [54]. As shown in Table 1, R_{ct} (0.267 Ω) and R_d (1.574 Ω) of AC-G2 were the lowest among all the cathodes. In Ge's study, the R_{ct} of Co_3O_4 and NiCo_2O_4 were 0.9369 Ω , 0.7926 Ω , respectively, higher than $\beta\text{-Ga}_2\text{O}_3/\text{AC}$ [26, 55]. Besides, the R_{ct} of $\beta\text{-Ga}_2\text{O}_3/\text{AC}$ was much smaller than Cu/AC (1.318 Ω) and three-dimensional Cu_xO (1.064 Ω) [9, 56]. The result of EIS indicated that the treatment of doping $\beta\text{-Ga}_2\text{O}_3$ could accelerate the charge transfer process. In short, the introduction of $\beta\text{-Ga}_2\text{O}_3$ not only decreased the R_d but also enhanced diffusion of both H^+ and oxygen, which demonstrated the improvement of the ORR performance (Table 2).

Performance of MFC

In order to obtain a mature anodic biofilm and stable potential output that could evaluate the performance of MFC, polarization curves and power density curves were collected after one month. The composition of the biofilm was measured and the result was shown in Fig. S4. It was obvious that the composition of the biofilm were mainly bacteroidetes, firmicutes, and proteobacteria.

The results of power densities were presented in Fig. 4a and Table 3, which indicated that the doping of $\beta\text{-Ga}_2\text{O}_3$ has significant effect on the performance of MFCs. From the overall trend, the power density rose up to a maximum and then decreased by manifolds with the doping ratio of $\beta\text{-Ga}_2\text{O}_3$ increased from 0% to 8%, and the power density exhibited a positive trend: RAW-AC < AC-G3 < AC-G1 < AC-G2. The maximum power density obtained by the air cathode AC-G2 was almost three times higher than that of RAW-AC. This

Table 1 Fitting results of different cathodes based on the equivalent circuit

	RAW-AC	AC-G1	AC-G2	AC-G3
R_0 (Ω)	14.530	9.430	9.318	11.840
R_d (Ω)	3.538	1.943	1.574	1.914
R_{ct} (Ω)	1.001	0.864	0.267	0.269
R_T (Ω)	19.069	12.237	11.157	14.023

Table 2 Power densities of different cathodes in this work

	RAW-AC	AC-G1	AC-G2	AC-G3
Power density (mW m^{-2})	630 ± 40	1672 ± 40	1843 ± 40	1640 ± 40

power density was 73% higher compared with that of the MFC with Pt/C cathode (1060 mW m^{-2}), and it was also 46% higher than that of the Pt/C control cathode with electro-deposition ($1260 \pm 40 \text{ mW m}^{-2}$) (Fig. S5) [39]. As shown in Fig. 4b, the anode potentials were almost similar, indicating that the polarization resistance of anode was resembtant while there is a tremendous difference in cathodes. Accordingly, the performance of air cathode was mainly responsible for improving the power output, while the anode exerted an insignificant effect on the power output.

The power densities of modified cathodes reported in literature were shown in Table 4. The reported semiconductor modified cathode, such as the nano Fe_3O_4 , carnation-like MnO_2 and N -type Cu_2O , generated the maximum power

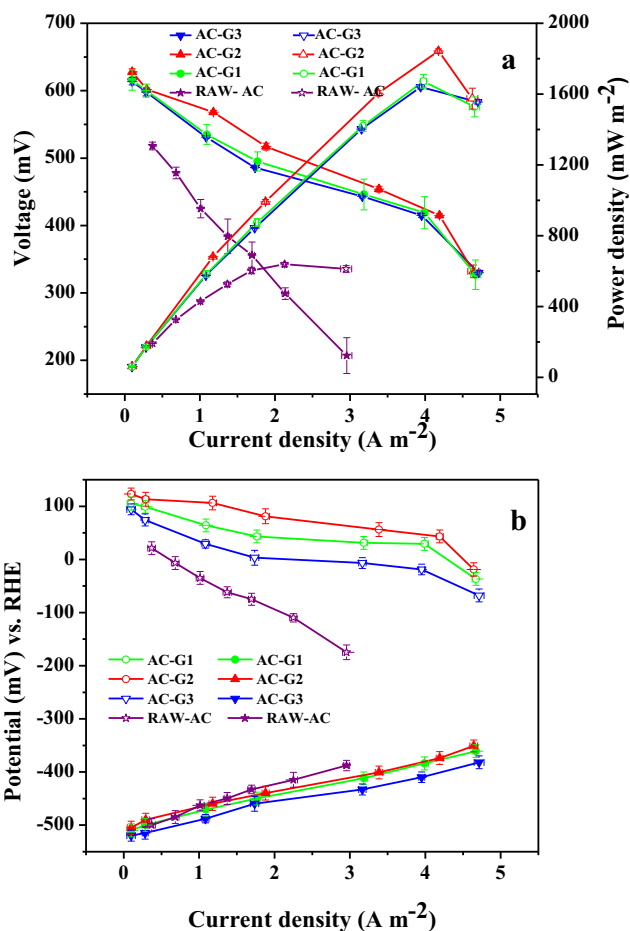


Fig. 4 a Polarization and power density curves; b individual polarization curve of cathode and anode

Table 3 Comparison of reported power densities of modified cathodes

The air cathode	Power density (mW m^{-2})	Ref.
Fe_3O_4	1430	[8]
MnO_2	1554	[10]
<i>N</i> -type Cu_2O	1390	[9]
Co_3O_4	1500	[55]
NiCo_2O_4	1730	[26]
Ni-ACFs/CNFs	1145	[57]

density of 1430 mW m^{-2} , 1554 mW m^{-2} and 1390 mW m^{-2} , respectively [8–10]. For other non-precious metals, the maximum power density were 1500 mW m^{-2} (Co_3O_4 modified MFC) and 1730 mW m^{-2} (urchin-like NiCo_2O_4 modified MFC), respectively [26, 55]. Besides, MFC with Ni nanoparticles-dispersed carbon produced a maximum power density, which reached 1145 mW m^{-2} [57]. Moreover, in order to further improve the performance of MFCs, it was highly necessary to enhance the performance of anode materials. Zhang et al. reported that the MFCs with the polypyrrole (PPy) nanotube membrane anode achieved its maximum power density of 612 mW m^{-2} [58]. Throughout these studies, MFCs equipped with $\beta\text{-Ga}_2\text{O}_3$ got the higher power density. Thus $\beta\text{-Ga}_2\text{O}_3$ was a promising catalyst for the MFCs.

Catalysis kinetics on ORR

Tafel plots of four air cathodes were shown in Fig. 5a, and a linear region (overpotential of 280–300 mV with $R^2 > 0.99$) was extracted and the corresponding curves were shown in the insert image. The linear fitting results were listed in Table 2.

The exchange current densities were ordered as following: AC-G2 ($17.584 \times 10^{-4} \text{ A cm}^{-2}$) $>$ AC-G1 ($17.398 \times 10^{-4} \text{ A cm}^{-2}$) $>$ AC-G3 ($16.085 \times 10^{-4} \text{ A cm}^{-2}$) $>$ RAW-AC ($5.592 \times 10^{-4} \text{ A cm}^{-2}$). Compared with RAW-AC , the i_0 of AC-G2 increased by 3.144 times, indicating an excellent performance to ORR. In previous reports, the i_0 of nano Fe_3O_4 and Co_3O_4 were $18.710 \times 10^{-4} \text{ A cm}^{-2}$ and $18.865 \times 10^{-4} \text{ A cm}^{-2}$ respectively, which were similar to $\beta\text{-Ga}_2\text{O}_3$ [8, 55]. The i_0 of

Table 4 Exchange current density calculated from the Tafel plots

The air cathode	Linear fitting equation (R^2)	$10^{-4}i_0$ (A cm^{-2})
AC	$y = 4.7033x - 3.2524$ (0.9987)	5.592
AC-G1	$y = 5.1501x - 2.7595$ (0.9978)	17.398
AC-G2	$y = 5.0442x - 2.7549$ (0.9979)	17.584
AC-G3	$y = 5.2459x - 2.7936$ (0.9977)	16.085

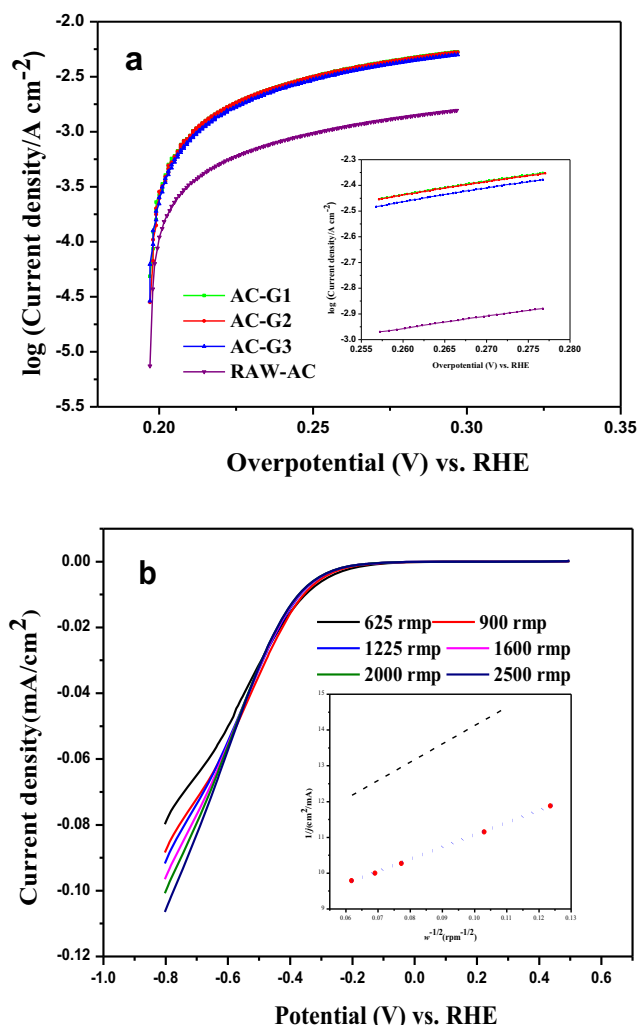


Fig. 5 a Tafel plots of different cathodes. The potential window ranges from open circuit potential to the overpotential of 300 mV at 1 mV s^{-1} and b rotating disk voltammograms of the $\beta\text{-Ga}_2\text{O}_3$ in O_2 -saturated PBS electrolyte and the Koutecky-Levich plot (red line) at the potential of -0.8 V (j^{-1} vs. $\omega^{-1/2}$). The dashed lines show the theoretical plots for 4e- (blue) and 2e- (black) transfers respectively

CoGa_2O_4 was little bigger than $\beta\text{-Ga}_2\text{O}_3$ [32]. While the i_0 of $\beta\text{-Ga}_2\text{O}_3$ was much higher than that of Cu_xO ($13.827 \times 10^{-4} \text{ A cm}^{-2}$) and Cu_2O ($10.030 \times 10^{-4} \text{ A cm}^{-2}$) [9, 56]. The Tafel analysis was in accordance with the LSV and EIS results, which were investigated above. The results suggested that doping appropriate amount of $\beta\text{-Ga}_2\text{O}_3$ could reduce resistance and accelerate the kinetics [59].

The RDE measurements were used to further research ORR kinetics and the associated reaction mechanism. The number of electron transfer of $\beta\text{-Ga}_2\text{O}_3$ during ORR was calculated by the Koutecky-Levic (K-L) equation [60]. Figure 5b and S6 showed the rotating disk voltammograms of $\beta\text{-Ga}_2\text{O}_3$ and AC. The linearity of K-L plots indicated first-order reaction kinetics toward the concentration of dissolved oxygen which was illustrated in insert image. On the basis of the line slope, the electron transfer number (n) values were 3.8 and 2.1

for β -Ga₂O₃/AC and AC in the potential range of 0.5 to – 0.8 V, respectively, indicating that ORR dominantly proceeded through four-electron and two-electron reaction pathway, respectively. Compared to two-electron process, four-electron process was more instrumental to ORR process, which has been reported in the literature [61]. Assumpção's study showed that n in the ORR for different carbon materials Printex L6 and Vulcan XC-72R were 2.2 and 2.9, respectively [60]. In previous report, the n value of MnO₂ (30%)/CNT was 3.02 while MnCo₂O₄/C was 3.5, both were lower than β -Ga₂O₃/AC, which indicated that the ORR could be easily transpired on the catalysts [62, 63]. The higher value of n of β -Ga₂O₃ implied a more efficient pathway to reduce oxygen. The RDE features suggested that four-electron process facilitate the ORR on β -Ga₂O₃/AC electrode.

Conclusion

Nanorod semiconductor metal oxide (β -Ga₂O₃), which was synthesized with a simple hydrothermal method, was effectively used to modify AC air cathode single chamber MFC to generate power. The electrochemical characterization showed that the total resistance of the electrode was reduced, and ORR acted by a four-electron pathway. The high rate oxygen vacancy and mesoporous surface area of β -Ga₂O₃ achieved the improvement of catalytic performance. The modified MFC achieved the maximum power density $1843 \pm 40 \text{ mW m}^{-2}$, about three times higher than the control. Consequently, the β -Ga₂O₃ is a promising catalyst material for MFCs application.

Funding information This work was supported by the National Science Foundation of Tianjin (17JCYBJC23300), National Key R&D Program of China (No. 2016YFC 0400704 and No. 2016YFC0401407), and the Open Research Fund of State Key Laboratory of Simulation and Regulation of Water Cycle in River Basin (No. IWHR-SKL-KF201806).

References

- Zhang X, He W, Yang W, Liu J, Wang Q, Liang P, Huang X, Logan BE (2016) Diffusion layer characteristics for increasing the performance of activated carbon air cathodes in microbial fuel cells. *Environ Sci Water Res Technol* 2(2):266–273
- Yang W, Kim KY, Logan BE (2015) Development of carbon free diffusion layer for activated carbon air cathode of microbial fuel cells. *Bioresour Technol* 197:318–322
- Li WW, Yu HQ, He Z (2013) Towards sustainable wastewater treatment by using microbial fuel cells-centered technologies. *Energy Environ Sci* 7(3):911–924
- Ce Z, Chen J, Ding Y, Wang VB, Bao B, Kjelleberg S, Cao B, Loo SCJ, Wang LH, Huang W, Zhang Q (2015) Chemically functionalized conjugated oligoelectrolyte nanoparticles for enhancement of current generation in microbial fuel cells. *ACS Appl Mater Interfaces* 7:14501–14505
- Zhang B, Wen Z, Ci S, Mao S, Chen J, He Z (2014) Synthesizing nitrogen-doped activated carbon and probing its active sites for oxygen reduction reaction in microbial fuel cells. *ACS Appl Mater Interfaces* 6(10):7464–7470
- Puzzo DP, Helander MG, O'Brien PG, Wang Z, Soheilnia N, Kherani N, Lu Z, Ozin GA (2011) Organic light-emitting diode microcavities from transparent conducting metal oxide photonic crystals. *Nano Lett* 11(4):1457–1462
- Wang J, Wu B, Zhang G, Tian L, Gu G, Gao C (2016) Pressure induced semiconductor–metal phase transition in GaAs: experimental and theoretical approaches. *RSC Adv* 6(12):10144–10149
- Fu Z, Yan L, Li K, Ge B, Pu L, Zhang X (2015) The performance and mechanism of modified activated carbon air cathode by non-stoichiometric nano Fe₃O₄ in the microbial fuel cell. *Biosens Bioelectron* 74:989–995
- Zhang X, Li K, Yan P, Liu Z, Pu L (2015) N-type Cu₂O doped activated carbon as catalyst for improving power generation of air cathode microbial fuel cells. *Bioresour Technol* 187:299–304
- Zhang P, Li K, Liu X (2014) Carnation-like MnO₂ modified activated carbon air cathode improve power generation in microbial fuel cells. *J Power Sources* 264:248–253
- Guo DY, Zhao XL, Zhi YS, Cui W, Huang YQ, An YH, Li PG, Wu ZP, Tang WH (2016) Epitaxial growth and solar-blind photoelectric properties of corundum-structured α -Ga₂O₃ thin films. *Mater Lett* 164:364–367
- Lopez I, Cebriano T, Hidalgo P, Nogales E, Piqueras J, Méndez B (2016) The role of impurities in the shape, structure and physical properties of semiconducting oxide nanostructures grown by thermal evaporation. *AIMS Mater Sci* 3(2):425–433
- Wang LS, Xu JP, Liu L, Lu H, Lai P, Tang W (2015) Plasma-nitrided Ga₂O₃(Gd₂O₃) as interfacial passivation layer for InGaAs metal-oxide-semiconductor capacitor with HfTiON gate dielectric. *IEEE Trans Electron Devices* 62(4):1235–1240
- Li X, Zhen X, Meng S, Xian J, Shao Y, Fu X, Li D (2013) Structuring beta-Ga₂O₃ photonic crystal photocatalyst for efficient degradation of organic pollutants. *Environ Sci Technol* 47(17):9911–9917
- Zhang W, Naidu BS, Ou JZ, O'Mullane AP, Chrimes AF, Carey BJ, Wang Y, Tang S-Y, Sivan V, Mitchell A, Bhargava SK, Kalantar ZK (2015) Liquid metal/metal oxide frameworks with incorporated Ga₂O₃ for photocatalysis. *ACS Appl Mater Interfaces* 7(3):1943–1948
- Reddy LS, Ho YH, Yu JS (2015) Hydrothermal synthesis and photocatalytic property of β -Ga₂O₃ nanorods. *Nanoscale Res Lett* 10(1):364
- Quan Y, Fang D, Zhang X, Liu S, Huang K (2010) Synthesis and characterization of gallium oxide nanowires via a hydrothermal method. *Mater Chem Phys* 121(1–2):142–146
- Dong H, Yu H, Wang X, Zhou Q, Feng J (2012) A novel structure of scalable air-cathode without Nafion and Pt by rolling activated carbon and PTFE as catalyst layer in microbial fuel cells. *Water Res* 46(17):5777–5787
- Wang X, Gao N, Zhou Q, Dong H, Yu H, Feng Y (2013) Acidic and alkaline pretreatments of activated carbon and their effects on the performance of air-cathodes in microbial fuel cells. *Bioresour Technol* 144:632–636
- Liu H, Logan BE (2004) Electricity generation using an air-cathode single chamber microbial fuel cell in the presence and absence of a proton exchange membrane. *Environ Sci Technol* 38(14):4040–4046
- Lv Z, Xie D, Yue X, Feng C, Wei C (2012) Ruthenium oxide-coated carbon felt electrode: a highly active anode for microbial fuel cell applications. *J Power Sources* 210:26–31
- Feng C, Ma L, Li F, Mai H, Lang X, Fan S (2010) A polypyrrole/anthraquinone-2,6-disulphonic disodium salt (PPy/AQDS)-

- modified anode to improve performance of microbial fuel cells. *Biosens Bioelectron* 25(6):1516–1520
23. Zhao C, Wu J, Ding Y, Wang VB, Zhang Y, Kjelleberg S, Loo JSC, Cao B, Zhang Q (2015) Hybrid conducting bio-film with built-in bacteria for high-performance microbial fuel cells. *ChemElectroChem* 2(5):654–658
 24. He Z, Mansfeld F (2009) Exploring the use of electrochemical impedance spectroscopy (EIS) in microbial fuel cell studies. *Energy Environ Sci* 2(2):215–219
 25. Dong H, Yu H, Wang X (2012) Catalysis kinetics and porous analysis of rolling activated carbon-PTFE air-cathode in microbial fuel cells. *Environ Sci Technol* 46(23):13009–13015
 26. Ge B, Li K, Fu Z, Pu L, Zhang X, Liu Z, Huang K (2016) The performance of nano urchin-like NiCo₂O₄ modified activated carbon as air cathode for microbial fuel cell. *J Power Sources* 303:325–332
 27. Mohamed SH, El-Hagary M, Althoyaib S (2012) Growth of β -Ga₂O₃ nanowires and their photocatalytic and optical properties using Pt as a catalyst. *J Alloys Compd* 537:291–296
 28. Girija K, Thirumalairajan S, Mastelaro VR, Mangalaraj D (2016) Catalyst free vapor–solid deposition of morphologically different β -Ga₂O₃ nanostructure thin films for selective CO gas sensors at low temperature. *Anal Methods* 8(15):3224–3235
 29. Wei J, Zang Z, Xue C, Shi F (2014) Synthesis of β -Ga₂O₃ nanorods by catalyzed chemical vapor deposition and their characterization. *J Mater Sci Mater Electron* 26:1368–1373
 30. Liu J, Zhang G (2015) Mesoporous mixed-phase Ga₂O₃: green synthesis and enhanced photocatalytic activity. *Mater Res Bull* 68:254–259
 31. Wang B, Huang J, Wang L, Shan W, Wang S (2012) Mesoporous copper–cerium–oxygen hybrid nanostructures for low temperature catalytic oxidation of carbon monoxide. *J Porous Mater* 20:629–635
 32. Liu D, Mo X, Li K, Liu Y, Wang J, Yang T (2017) The performance of spinel bulk-like oxygen-deficient CoGa₂O₄ as an air-cathode catalyst in microbial fuel cell. *J Power Sources* 359:355–362
 33. Liu Y, Li K, Ge B, Pu L, Liu Z (2016) Influence of micropore and mesoporous in activated carbon air-cathode catalysts on oxygen reduction reaction in microbial fuel cells. *Electrochim Acta* 214:110–118
 34. Hou J, Liu Z, Yang S, Zhou Y (2014) Three-dimensional macroporous anodes based on stainless steel fiber felt for high-performance microbial fuel cells. *J Power Sources* 258:204–209
 35. Yu H, Fisher A, Cheng D, Cao D (2016) Cu, N-codoped hierarchical porous carbons as electrocatalysts for oxygen reduction reaction. *ACS Appl Mater Interfaces* 8(33):21431–21439
 36. Li G-P, Weng W, Li F-M (2015) Photocatalytic performance of α - and β -Ga₂O₃ for the degradation of tetracycline hydrochloride in water. *Chin J Struct Chem* 34:1779–1785
 37. Patra CR, Mastai Y, Gedanken A (2004) Microwave-assisted synthesis of submicrometer GaO(OH) and Ga₂O₃ rods. *J Nanopart Res* 6(5):509–518
 38. Su FZ, Ni J, Sun H, Cao Y, He YH, Fan KN (2008) Gold supported on nanocrystalline β -Ga₂O₃ as a versatile bifunctional catalyst for facile oxidative transformation of alcohols, aldehydes, and acetals into esters. *Chemistry* 14(24):7131–7135
 39. Zhang F, Cheng S, Pant D, Bogaert GV, Logan BE (2009) Power generation using an activated carbon and metal mesh cathode in a microbial fuel cell. *Electrochem Commun* 11(11):2177–2179
 40. Girija K, Thirumalairajan S, Mangalaraj D (2014) Morphology controllable synthesis of parallelly arranged single-crystalline β -Ga₂O₃ nanorods for photocatalytic and antimicrobial activities. *Chem Eng J* 2014(236):181–190
 41. Pan Y-X, Sun Z-Q, Cong H-P, Men Y-L, Xin S, Song J, Yu S-H (2016) Photocatalytic CO₂ reduction highly enhanced by oxygen vacancies on Pt-nanoparticle-dispersed gallium oxide. *Nano Res* 9(6):1689–1700
 42. Chang LW, Chang JH, Yeh JW, Lin HN, Shih HC (2011) Zigzag GaN/Ga₂O₃ heterogeneous nanowires: synthesis, optical and gas sensing properties. *AIP Adv* 1(3):032114
 43. Zhu Y, Zhou W, Yu J, Chen Y, Shao Z, Liu M (2016) Enhancing electrocatalytic activity of perovskite oxides by tuning cation deficiency for oxygen reduction and evolution reactions. *Chem Mater* 28(6):1691–1697
 44. Thomas SR, Adamopoulos G, Lin Y-H, Faber H, Sygellou L, Stratakis E (2014) High electron mobility thin-film transistors based on Ga₂O₃ grown by atmospheric ultrasonic spray pyrolysis at low temperatures. *Appl Phys Lett* 105(9):092105
 45. Wang C, Wu D, Wang P, Ao Y, Hou J, Qian J (2015) Effect of oxygen vacancy on enhanced photocatalytic activity of reduced ZnO nanorod arrays. *Appl Surf Sci* 325:112–116
 46. Ma Y, Wang R, Wang H, Key J, Ji S (2015) Control of MnO₂ nanocrystal shape from tremella to nanobelt for enhancement of the oxygen reduction reaction activity. *J Power Sources* 280:526–532
 47. Sengodan S, Choi S, Jun A, Shin TH, Ju YW, Jeong HY, Shin J, Irvine JTS, Kim G (2015) Layered oxygen-deficient double perovskite as an efficient and stable anode for direct hydrocarbon solid oxide fuel cells. *Nat Mater* 14(2):205–209
 48. Zheng Z, Fang Z, Ye X, Yao X, Fu X, Lin S, Liu P (2015) A visualized probe method for localization of surface oxygen vacancy on TiO₂: Au in situ reduction. *Nanoscale* 7:17488–17495
 49. Kang BK, Lim HD, Mang SR, Song KM, Jung MK, Kim S-W, Yoon DH (2015) Synthesis and characterization of monodispersed beta-Ga₂O₃ nanospheres via morphology controlled Ga₄(OH)₁₀SO₄ precursors. *Langmuir* 31(2):833–838
 50. Yang T, Li K, Pu L, Liu Z, Ge B, Pan Y, Liu Y (2016) Hollow-spherical Co/N-C nanoparticle as an efficient electrocatalyst used in air cathode microbial fuel cell. *Biosens Bioelectron* 86:129–134
 51. Guo XC, Hao NH, Guo DY, Wu ZP, An YH, Chu XL, Li LH, Li PG, Lei M, Tang WH (2016) β -Ga₂O₃/p-Si heterojunction solar-blind ultraviolet photodetector with enhanced photoelectric responsivity. *J Alloys Compd* 660:136–140
 52. Hisatomi T, Kubota J, Domen K (2014) Recent advances in semiconductors for photocatalytic and photoelectrochemical water splitting. *Chem Soc Rev* 43(22):7520–7535
 53. Li X, Wen J, Low J, Fang Y, Yu J (2014) Design and fabrication of semiconductor photocatalyst for photocatalytic reduction of CO₂ to solar fuel. *Sci China Mater* 57:70–100
 54. Wen Q, Wang S, Yan J, Cong L, Pan Z, Ren Y, Fan Z (2012) MnO₂–graphene hybrid as an alternative cathodic catalyst to platinum in microbial fuel cells. *J Power Sources* 216:187–191
 55. Ge B, Li K, Fu Z, Pu L, Zhang X (2015) The addition of ortho-hexagon nano spinel Co₃O₄ to improve the performance of activated carbon air cathode microbial fuel cell. *Bioresour Technol* 195:180–187
 56. Liu Z, Li K, Zhang X, Ge B, Pu L (2015) Influence of different morphology of three-dimensional Cu_xO with mixed facets modified air-cathodes on microbial fuel cell. *Bioresour Technol* 195:154–161
 57. Singh S, Verma N (2015) Fabrication of Ni nanoparticles-dispersed carbon micro-nanofibers as the electrodes of a microbial fuel cell for bio-energy production. *Int J Hydrog Energy* 40(2):1145–1153
 58. Zhao CE, Wu J, Kjelleberg S, Loo JSC, Zhang Q (2015) Employing a flexible and low-cost polypyrrole nanotube membrane as an anode to enhance current generation in microbial fuel cells. *Small* 11(28):3440–3443
 59. Jadhav DA, Ghadge AN, Mondal D, Ghangrekar MM (2014) Comparison of oxygen and hypochlorite as cathodic electron acceptor in microbial fuel cells. *Bioresour Technol* 154:330–335

60. Assumpção M, De Souza RFB, Rascio DC, Silva JCM, Calegari ML, Gaubeur I, Paixão TRLC, Hammer P, Lanza MRV, Santosa MC (2011) A comparative study of the electrogeneration of hydrogen peroxide using Vulcan and Printex carbon supports. *Carbon* 49(8):2842–2851
61. Tian P, Liu D, Li K, Yang T, Wang J, Liu Y, Zhang S (2017) Porous metal-organic framework Cu₃(BTC)₂, as catalyst used in air-cathode for high performance of microbial fuel cell. *Bioresour Technol* 244(Pt 1):206–212
62. Chen Y, Lv Z, Xu J, Peng D, Liu Y, Chen J, Sun X, Feng C, Wei C (2012) Stainless steel mesh coated with MnO₂/carbon nanotube and polymethylphenyl siloxane as low-cost and high-performance microbial fuel cell cathode materials. *J Power Sources* 201:136–141
63. Khilari S, Pandit S, Das D, Pradhan D (2014) Manganese cobaltite/polypyrrole nanocomposite-based air-cathode for sustainable power generation in the single-chambered microbial fuel cells. *Biosens Bioelectron* 54:534–540

Publisher's note Springer Nature remains neutral with regard to jurisdictional claims in published maps and institutional affiliations.